ARTICLE

Tailoring the Structure and Self-Activated Photoluminescence of Carbonated Amorphous Calcium Phosphate Nanoparticles for Bioimaging Applications†

Received 00th January 20xx,
Accepted 00th January 20xx

DOI: 10.1039/x0xx00000x

Thales R. Machado,[*a] Carlos E. Zanardo,[a] Raquel R.C. Vilela,[a] Renata R. Miranda,[a] Natália S. Moreno,[a] Celisnolia M. Leite,[a] Elson Longo,[b] and Valtencir Zucolotto[*a]

Self-activated luminescent calcium phosphate (CaP) nanoparticles, including hydroxyapatite (HA) and amorphous calcium phosphate (ACP), are promising for bioimaging and theragnostic applications in nanomedicine, eliminating the need for activator ions or fluorophores. In this study, we developed luminescent and stable citrate-functionalized carbonated ACP nanoparticles for bioimaging purposes. Our findings revealed that both the CO_3^{2-} content and the posterior heating step at 400 °C significantly influenced the composition and the structural ordering of the chemically precipitated ACP nanoparticles, impacting the intensity, broadness, and position of the defect-related photoluminescence (PL) emission band. The heat-treated samples also exhibited excitation-dependent PL under excitation wavelengths typically used in bioimaging (λ_{exc} = 405, 488, 561, and 640 nm). Citrate functionalization improved the PL intensity of the NPs by inhibiting non-radiative deactivation mechanisms in solution. Additionally, it resulted in an increased colloidal stability and reduced aggregation, high stability of the metastable amorphous phase and the PL emission for at least 96 h in water and supplemented culture medium. MTT assay of HepaRG cells, incubated for 24 and 48 h with the nanoparticles in concentrations ranging from 10 to 320 μg.mL^{-1}, evidenced their high biocompatibility. Internalization studies using the nanoparticles self-activated PL showed that cellular uptake of the nanoparticles is both time (4–24 h) and concentration (160–320 μg.mL^{-1}) dependent. Experiments using confocal laser scanning microscopy allowed the successful imaging of the NPs inside cells via their intrinsic PL after 4 h of incubation. Our results highlight the potential use of citrate-functionalized carbonated ACP nanoparticles to be used in internalization assays and bioimaging procedures.

Introduction

Calcium phosphates (CaPs) are highly valued materials in the biomedical field due to their exceptional biocompatibility, biodegradability, and bioactivity.[1] Furthermore, CaP nanoparticles (NPs) composed of hydroxyapatite (HA) and amorphous calcium phosphates (ACPs) stand out as promising nanocarriers for targeted delivery of drugs, genes, and proteins in nanomedicine applications.[2,3] These NPs offer advantages such as tunable biodegradability, pH-responsive behavior, high loading capacity of bioactive molecules, facile preparation and functionalization.[4,5] Notably, HA and ACP can also be modified with luminescent ions (e.g., Eu^{3+}, Tb^{3+}, Sm^{3+}) for various bioimaging applications, biosensing, and imaging-guided drug delivery systems.[6–9] An intriguing feature of HA NPs is their high structural flexibility, which allows the stabilization of diverse structural and point defects for the optimization of self-activated photoluminescence (PL) emission.[10] The latter offers a promising avenue to create a new class of biocompatible luminescent materials for various fluorescence imaging and theragnostic applications in nanomedicine,[11–15] which advantages include the simpler preparation methods of the luminescent HA NPs that eliminate the need for activator ions or fluorophores. However, while the mechanisms underlying these luminescent properties and possible applications have been extensively studied in HA NPs, further investigations are required to gain comprehensive understanding of this phenomenon in ACP, and thus explore its potential uses in nanomedicine.

ACPs are amorphous CaP phases consisting of Ca^{2+} cations and orthophosphate anions with different protonation states with a significantly amount of structural water molecules.[16] Among them, amorphous tricalcium phosphate (ATCP) represents a typical ACP structure, characterized as a long-range disordered phase with short- and medium-range order, resulting from the random arrangement of $Ca_9(PO_4)_6$ building blocks known as Posner's clusters.[17] ATCP exhibits a Ca/P molar ratio of 1.5 and approximately 15 wt.% of structural water content inside the particles (Ca/H_2O = 1), leading to a general stoichiometry of $Ca_3(PO_4)_2.3H_2O$.[18] However, during the typical preparation procedure of ACP particles under conditions of pH ranging from 9.5 to 10.5, hydrogen phosphate (HPO_4^{2-}) can

[a] GNANO - Nanomedicine and Nanotoxicology Group, Physics Institute of São Carlos, University of São Paulo, 13566-590 São Carlos, SP, Brazil.
[b] CDMF - Center for the Development of Functional Materials, Federal University of São Carlos, 13565-905 São Carlos, SP, Brazil.
[c] *Corresponding authors. E-mail: trmachado@ifsc.usp.br, zuco@ifsc.usp.br
†Electronic Supplementary Information (ESI) available: See DOI: 10.1039/x0xx00000x

replace phosphate (PO_4^{3-}) groups, generating calcium vacancies (V_{Ca}) and resulting in a Ca/P ratio ranging from 1.4 to 1.5.[16] Reports from the literature have shown a range of structural water contents varying from 9.5 to 16.8 wt.%.[19,20] ACP is considered a precursor phase in the formation of synthetic and biogenic HA, and exhibits several structural similarities with HA and other CaPs.[2] However, due to their lack of long-range order (LRO), high water content and density of defects, ACPs demonstrate the highest degradability and more prominent pH-responsive performance among CaP phases, making them favorable for various applications in biomedical field.[21] Furthermore, our preliminary study demonstrated that the lattice disorder and defects in chemically-precipitated ACP NPs heat-treated at 400 °C gives rise to intense self-activated broadband PL emission in the visible region.[22]

In addition to doping with luminescent ions, various ions such as Mg^{2+}, Ba^{2+}, Fe^{3+}, and CO_3^{2-} can be stabilized in ACP NPs, affecting their properties including short-range order (SRO), solubility, and stability.[23] Specifically, in the preparation of ACP under normal conditions, slight amounts of carbonates are naturally present, replacing phosphate groups and generating V_{Ca} vacancies.[24] Upon adjusting the pH value or modifying the initial $[CO_3]/[PO_4]$ molar ratios, carbonated ACP samples with varying degrees of carbonation (up to ~20 wt.%) can be obtained, leading to ACP particles with Ca/P ratios greater than 1.5.[16,25] The incorporation of carbonates, up to ~23 wt.%, can also occur in HA during precipitation, depending on the same parameters.[26] Carbonates are also present in biogenic HA nanocrystals, in which variable amounts of this impurity is present in bones (~4–6 wt.%).[27] Extensive literature exists on the detailed information regarding the role of carbonates on the structure, morphology, and properties of bioapatite and synthetic carbonated HA NPs.[28] The influence of CO_3^{2-} groups and associated defects on the self-activated PL of HA NPs has also been demonstrated.[29–32] However, comprehensive structural studies on carbonated ACP are limited, and the relationship between CO_3^{2-} impurities concentration and the intrinsic PL properties of ACPs has not been previously considered.

This study presents a comprehensive analysis of the relationship between the structural changes and intrinsic PL properties of chemically-precipitated ACP NPs as a function of the degree of carbonation and subsequent heat treatment step at 400 °C. Also, we aimed at confirming the applicability of the optimized carbonated ACP NPs in nanomedicine based on the self-activated PL properties. However, it should be noted that ACP NPs are metastable in solution and tend to convert into calcium deficient carbonated HA over a short period of time.[16,22] To overcome this issue, we employed a functionalization strategy using citrate ions. These biocompatible species, constituting approximately 5.5 wt.% of the total organic components in bones, exhibit a strong affinity for both synthetic and biogenic HA NP surfaces, influencing their crystallization pathways from ACP precursors and assembly mechanisms.[33–38] Citrate ions also play a crucial role in maintaining stable colloidal suspensions of HA NPs,[39] and serve as stabilizing agents for amorphous ACP phases in aqueous solutions.[40–42] Previous studies have demonstrated the preparation and application of citrate-based self-activated luminescent HA NPs,[14] as well as biomimetic citrate-coated luminescent HA doped with Eu^{3+} or Tb^{3+},[43–45] in drug delivery and bioimaging. Luminescent Eu^{3+}-doped ACP NPs stabilized by citrates have been used for creatinine quantification.[9] Herein, we investigate the influence of citrate on the self-activated PL of ACP NPs, optimized through carbonates incorporation and heat treatment, along with its effect on stabilizing the amorphous phase and the colloidal suspensions in aqueous media, aiming for bioimaging applications.

Experimental Section

Synthesis of carbonated ACP NPs

Carbonated ACP NPs were synthesized via chemical precipitation method at room temperature. This involved adding 100 mL of an aqueous solution of di-ammonium phosphate ($(NH_4)_2HPO_4$, Sigma Aldrich) with a concentration of 0.06 M and pH 10 into 50 mL of an aqueous solution of calcium nitrate tetrahydrate ($Ca(NO_3)_2.4H_2O$, Sigma Aldrich) with a concentration of 0.18 M and pH 10. The pH of both solutions was adjusted using ammonium hydroxide (NH_4OH, Synth). The resulting milky suspension was stirred for 1 min and then separated by centrifugation (6000 rpm/1 min). The resulting pellet of NPs was washed by redispersing them using a vortex mixer, followed by centrifugation under the same conditions. This procedure was repeated twice with water (160 mL) and acetone (60 mL), followed by drying overnight in an oven at 60 ^oC. The dried pellet was ground using an agate mortar and pestle without sieving and then stored at 4 °C. This sample was referred to as ACP1. To intentionally introduce CO_3^{2-} impurity, ammonium carbonate ($(NH_4)_2CO_3$, Sigma Aldrich) was added to the $(NH_4)_2HPO_4$ solution at different $[CO_3]/[PO_4]$ molar ratios (0.0625, 0.125, 0.25, 0.5, 1, 2, and 4) while maintaining a Ca/P molar ratio of 1.5. These samples were labeled as ACP2 to ACP8, respectively. The main synthesis parameters are summarized in Table S1. The as-synthesized ACP samples were further subjected to heat treatment at 400 °C/4 h using a programmable furnace with a heating rate of 10 °C/min, resulting in ACPx-HT samples, where x = 1 to 8 and HT = heat-treated. Samples were prepared in duplicate and subsequently characterized.

Compositional analysis

The carbonate weight percentage (wCO_3) in each as-synthesized and heat-treated ACP sample was determined using Fourier transform infrared (FTIR) spectroscopy. The ratio $r_{c/p}$, calculated as the integrated areas of the observed ν_3CO_3 and ν_1,ν_3PO_4 bands (Figure 1(c,d)), was used to quantify wCO_3 according to the methodology described by Grunenwald et al.[46] (see Figure S1 for detailed procedure). The wCO_3 of two representative samples were also estimated by elemental analysis using a CE Instruments Fisons-EA1108. The calcium and phosphorous weight percentages (wCa and wP, respectively) were estimated using inductively coupled plasma-optical

emission spectroscopy (ICP-OES) with a Perkin Elmer Avio 550 Max analyzer. The weight percentage of structural water ($wH_2O(S)$) in our samples was determined using thermogravimetric analysis (TGA) with an TA Instruments SDT-Q600. Approximately 5 mg of NPs were placed in an alumina crucible, and the analysis was conducted in a temperature range of 25–1000 °C at a heating rate of 10 °C/min under synthetic air.

Structure and photoluminescence

The structural characterization of the as-synthesized and heat-treated carbonated ACP NPs was performed using X-ray diffraction (XRD) analysis on a Rigaku Ultima IV instrument with CuKα radiation. The diffraction patterns were recorded in the 20–80° range with a step size of 0.02° and a scan rate of 5 °/min. Additionally, the structure of ACP samples was analyzed by recording FTIR spectra at room temperature. The FTIR spectra were collected using a Thermo Scientific Nicolet iS50 spectrometer, over the range of 4000–400 cm^{-1}, with a resolution of 4 cm^{-1} and 32 accumulations. The spectra were collected in transmittance mode and automatically converted to absorbance using the equation A = -log(T), where A is the absorbance and T the transmittance. The spectra were baseline corrected and normalized to the ν_3PO_4 mode with the highest absorbance value using the OMINIC 9 software. Subsequently, the ν_3PO_4 and ν_4PO_4 bands were integrated using the integration function of Origin 2022b software. This enabled the determination of the full width at half maximum (FWHM) parameter for these bands, providing insight into the degree of short-range ordering in the ACP structure.[22] The second derivative analysis was conducted using Origin 2022b software, following the procedure outlined by Uskoković.[47]

The self-activated PL properties of as-synthesized and heat-treated ACP powders were investigated using a Horiba Jobin Ivon spectrofluorometer, model Fluorolog-3, equipped with a Hamamatsu R928 photomultiplier. A continuous-wave Xenon arc lamp (450 W) was used as the excitation source. The measurements were conducted at an angle of 22.5° (front face), and the samples were excited at λ_{exc} = 405, 488, 561, and 640 nm. All PL emission intensities (photon counting) were corrected for the system spectral response. The deconvolution of ACP3 and ACP3-HT spectra at λ_{exc} = 405 nm was performed in Origin 2022b software following baseline correction. This was achieved using the multiple peak fit tool employing the Voigt function. Moreover, the integrated areas of the baseline-corrected emission bands at λ_{exc} = 405 nm were calculated using the integration function of Origin 2022b software. Luminescence decay curves were recorded using the same spectrofluorometer. For the lifetime (τ) in ns order, a Horiba Nanoled (λ_{exc} = 405 nm, frequency = 20 kHz) was employed as an excitation source, while the τ in ms order was measured using a pulsed Xe lamp at 405 nm. For a quantitative estimation, a multi-exponential decay function, Equation 1, was used, where A_i and τ_i represent the amplitudes and lifetimes, respectively. The average lifetime was given by Equation 2.

$$I(t) = \sum_i A_i e^{-\frac{t}{\tau_i}} \quad (1)$$

$$\tau_{avg} = \frac{\sum A_i \tau_i^2}{\sum A_i \tau_i} \quad (2)$$

Photoluminescence quantum yields were measured with a Quantaurus-QY Plus UV-NIR absolute PL quantum yield spectrometer (C13534) equipped with a Xenon light source (150 W), a spectralon integrating sphere as sample chamber, and a CCD detector in the range of 300 to 950 nm (Hamamatsu Photonics, Ltd., Shizuoka, Japan). ACP3-HT NPs were measured in triplicate.

Citrate functionalization

To stabilize the ACP3-HT NPs dispersion with the optimized PL emission, they were functionalized with citrate ions. The process involved suspending the NPs at a concentration of 0.5 $mg.mL^{-1}$ in an aqueous solution of trisodium citrate (Na_3Cit, $Na_3C_6H_5O_7$, Sigma-Aldrich) at 24 mM and pH 7.4 and subjecting them to sonication in an ultrasound bath at 100% power for 10 min. The resulting suspension was stirred for 3 h, and then thoroughly washed with H_2O by centrifugation (12000 rpm/ 10 min) to remove the excess of citrate ions and those loosely interacting with surface of the ACP NPs. The sample was resuspended in water and subsequently subjected to freeze-drying. The resulting sample was labeled as Cit/ACP3-HT NPs.

The functionalization with citrate ions was confirmed using FTIR spectroscopy applied to the dried Cit/ACP3-HT NPs compared to ACP3-HT NPs. The amount of adsorbed citrate was determined using UV-Vis spectroscopy, following the analytical procedure stablished by Krukowski et al.[48] The calibration curve was generated by mixing 2 mL of Na_3Cit solutions (ranging from 0.25 to 5 mM) with 2 mL of 0.25 M HCl solution, and then recording the absorption spectra. The absorption peak at 210 nm, indicative of citrate carboxyl groups, was utilized to construct the curve (refer to Figure S2). Duplicate measurements were conducted for each concentration. To indirectly determine the amount of adsorbed citrate on our NPs, triplicate analyses were performed by measuring the concentration of free citrates in supernatants after functionalization and subtracting them from the initial input. Before analysis, aliquots were diluted fourfold, and resulting solutions were mixed with 2 mL of 0.25 M HCl. Measurements were carried out using a Hitachi U2008 spectrophotometer with a quartz cuvette.

The ACP3-HT and Cit/ACP3-HT NPs were resuspended in water using a ultrasound bath at 100% of power for 2 min at a concentration of 0.05 $mg.mL^{-1}$ for further characterization. The morphological features were characterized using transmission electron microscopy (TEM) with a FEI TECNAI G^2 F20 microscope operating at 200 kV. The size of the NPs was estimated using ImageJ software in distinct TEM images collected for both samples. The number of counting require for statistical analyses were 100 NPs. The mean particle size and size distribution (PDI) of ACP3-HT and Cit/ACP3-HT suspensions were determined by dynamic light scattering (DLS) using photon correlation

spectroscopy with a laser beam at a wavelength of 633 nm and a detection angle of 90°. The Zeta potential (ZP) of ACP3-HT and Cit/ACP3-HT NPs was determined by electrophoretic mobility. The NPs were resuspended in water at 1 mg.mL^{-1} (pH 10) using the same procedure. Additionally, the ZP of Cit/ACP3-HT NPs was examined across a pH range of 10 to 3 by adding 0.5 M HCl solution. These analyses were conducted in a Malvern Zetasizer Nano ZS instrument at a temperature of 25 °C.

Phase stability in liquid

ACP is a metastable material that spontaneously undergoes crystallization into HA when dispersed in aqueous media. Therefore, it is crucial to assess its stability over time in liquid environments. The experiment was conducted in four contexts, each involving NPs at a concentration of 1 mg.mL^{-1}: (i) ACP3-HT NPs dispersed in water, (ii) Cit/ACP3-HT NPs dispersed in water, (iii) Cit/ACP3-HT NPs dispersed in DMEM (Dulbecco's Modified Eagle Medium) supplemented with 10% (v/v) fetal bovine serum (FBS)(T = 37 °C), and (iv) Cit/ACP3-HT NPs dispersed in 1x phosphate-buffered saline (PBS) solution. The phase stability of the samples was evaluated by collecting FTIR spectra of NPs aliquots at various time intervals in contact with the respective liquid media. The collection process involved two centrifugation steps at 6000 rpm for 3 min. In the first step, the supernatant was removed, while in the second step, acetone was employed to accelerate the drying of the samples. It is important to note that the final centrifugation step was omitted for NPs dispersed in DMEM+10% FBS to prevent potential interference caused by acetone reacting with the medium. Subsequently, the aliquots were placed in an oven at 60 °C for 30 minutes and then analyzed via FTIR spectroscopy.

Photoluminescence in liquid

The PL properties of Cit/ACP3-HT NPs suspensions were investigated at excitation wavelengths of 488 and 561 nm, which were chosen for subsequent *in vitro* assays. Initially, the emission spectra of ACP3-HT and Cit/ACP3-HT NPs were recorded in water suspensions (pH 10) at a concentration of 1 mg.mL^{-1} to evaluate the effect of citrate functionalization on PL properties. Subsequently, we collected emission spectra of Cit/ACP3-HT NPs at various concentrations ranging from 0.0625 to 4 mg.mL^{-1} to study the influence of NPs concentration. The emission spectra were also obtained at time points t = 0, 4, or 96 h in NPs suspensions (1 mg.mL^{-1}) in water (pH 10), DMEM+10%FBS (pH 7.4), PBS buffer (pH 7.4), or acetate buffer (pH 5.0) to examine the effects of time, pH, and crystallization on PL properties. Additionally, PL spectra were recorded at an NPs concentration of 1 mg.mL^{-1} in Tris-HCl buffer (pH 7.4) with varying ionic strengths achieved by adjusting the NaCl+KCl salts concentration from 100 to 200 mM. The integrated areas of the baseline-corrected emission bands were estimated using the integration function of Origin 2022b software. The spectra were acquired using a Horiba Jobin Ivon Fluorolog-3 spectrofluorometer equipped with a Xe lamp (450 W).

Cytotoxicity assay

To assess the biocompatibility of Cit/ACP3-HT NPs, MTT assay was performed using human healthy liver cells (HepaRG) as a model. The cells were cultured in DMEM supplemented with 10% FBS at 37 °C and 5% CO_2. The cells were seeded into 96-well plates at a density of 1x10^6 cells.mL^{-1}. After 24 h, the culture medium was replaced with fresh complete medium containing dispersed Cit/ACP3-HT NPs at concentrations of 0, 10, 20, 40, 80, 160, and 320 μg.mL^{-1}, and the cells were incubated for 24 and 48 h. After the respective incubation periods, the culture medium containing nanoparticles was removed from each well, and 100 mL of 3-[4,5-dimethylthiazol-2-yl]-2,5-diphenyltetrazolium bromide (MTT) solution at a concentration of 0.5 mg.mL^{-1} was added. The plates were incubated for 1 h, followed by the removal of all liquid, washing with PBS, and the addition of 200 mL of dimethyl sulfoxide (DMSO) to completely dissolve the formazan crystals formed by the metabolism of MTT by the cells. Absorbance readings were taken at 570 nm using a SpectraMax M3 microplate reader (Molecular Devices). Cell viability was determined by comparing the absorbance values of the treatment groups with those of the control group. The experiments were performed in triplicate on three independent occasions. The obtained data were analyzed using one-way analysis of variance (ANOVA) followed by Dunnett's *post hoc* test.

Internalization assay

HepaRG cells were plated at a density 1.0x10^5 cells/well in 12-well plates for flow cytometry analysis. Cit/ACP3-HT NPs were incubated with the cells at final concentrations of 160 and 320 μg.mL^{-1} for 4 and 24 h. Afterward, the cells were washed with PBS, detached with trypsin-EDTA solution (Vitrocell), centrifuged, and resuspended in Sheath fluid (400 μL) for analysis in the flow cytometer (FACSCalibur; BD Biosciences), recording 15000 events. The fluorescence was quantified by Flowjo software. The negative control consisted of untreated cells. The experiment was performed in triplicate.

Bioimaging probes

The use of Cit/ACP3-HT NPs for cellular labeling based on their intrinsic PL properties was evaluated using confocal laser scanning microscopy (CLSM). HepaRG cells (1x10^5 cells.mL^{-1}) were plated onto 24-well plates, containing pre-sterilized round microscopy coverslips on the bottom. The cells were then incubated for 24 h at 37 °C (5% CO_2) to promote cell adhesion and recovery. Following, the culture medium in each well was replaced with complete medium containing dispersed Cit/ACP3-HT NPs at concentrations of 160 or 320 μg.mL^{-1}, and the cells were further incubated for 4 or 24 h. The cells were washed with PBS solution, fixed with 4% paraformaldehyde for 30 minutes, and washed again with PBS. The coverslips were then mounted onto glass slides using a mounting medium and left to dry for 24 h. The samples were analyzed using an LSM 900 inverted confocal microscope (Zeiss) with excitation wavelengths of 405, 488, and 561 nm. To assess the imaging capability of the NPs in the presence of other markers, the cells were also labeled with Hoechst33342 (nuclear staining). CSLM images of HepaRG control cells and cells co-incubated with

Cit/ACP3-HT NPs, taken under the same conditions, were analyzed to measure the difference between the cellular autofluorescence emission and the emission from internalized Cit/ACP3-HT NPs. For this purpose, the images were analyzed using the HSB color model, representing each pixel by three values: Hue, Saturation, and Brightness. Since the brightness value correlates to the light emission captured by the microscope camera, the average pixel brightness in the images (n = 4) was calculated using a Python script with the OpenCV Library.

Results and discussion

Composition of ACP NPs

The compositions of the carbonated ACP samples are summarized in Table 1. The as-synthesized NPs exhibited a range of wCO_3 from 0.97 wt.% (ACP1) to 26.71 wt.% (ACP8), indicating that the employed methodology successfully originated ACP samples with varying degrees of carbonation. These findings are consistent with previous literature, which has demonstrated the high capacity of ACP to undergo $PO_4^{3-} \rightarrow CO_3^{2-}$ substitution.[25] A slight decrease in wCO_3 was observed in all samples following the heat treatment at 400 °C, resulting in values ranging from 0.62 wt.% (ACP1-HT) to 23.38 wt.% (ACP8-HT). This observation suggests a slight sublimation of CO_3^{2-} impurity in the form of CO_2 after the heating step.[49] These findings align with those of Zyman et al.,[50] who recently utilized TGA and mass spectrometry to show that small quantities of structural CO_3^{2-} start to decompose at temperatures below 400 °C in ACP.

The wCa and wP contents of the as-synthesized carbonated ACP NPs were determined through ICP-OES analysis, which allowed the calculation of their Ca/P molar ratios. As summarized in Table 1, the Ca/P values of ACP1 (Ca/P = 1.46) and ACP2 (Ca/P = 1.47) were found to be slightly lower than those of amorphous tricalcium phosphate (ATCP, $Ca_3(PO_4)_2$, Ca/P = 1.5). This is attributed to the presence of V_{Ca} vacancies, resulting from the acidic phosphate (HPO_4^{2-}) substituting PO_4^{3-} groups during the preparation of ACP NPs under similar conditions (see the FTIR spectra in Figure S3).[16] Notably, there was a continuous increase in the Ca/P molar ratio as the wCO_3 content of samples increased, reaching its highest value of 2.24 in ACP8. This behavior is associated with the progressive incorporation of CO_3^{2-}, which replaces PO_4^{3-} groups while generating V_{Ca} vacancies, ultimately leading to an overall increase in the Ca/P molar ratio.[19] Moreover, the wCO_3 and the resulting Ca/P values due to CO_3^{2-} incorporation align closely with those documented in the literature,[19,51] confirming the feasibility of the FTIR-based quantification methodology for ACP NPs, as corroborated by elemental analysis (see Table S2) and elsewhere.[52]

In the subsequent step, TGA was performed on all as-synthesized NPs to quantify their structural water contents, $wH_2O(S)$. By examining the TGA curves and their first derivative (DTG), illustrated in Figure S4, a significant mass loss ranging from 19.2 to 23.1 wt.% was evident up to 400 °C. This thermal event is mainly attributed to the reversible liberation of adsorbed water molecules and to the irreversible liberation of tightly bounded structural water, with the release extending to higher temperatures for the latter.[2,23,53] Based on these findings, we selected an initial temperature of 100 °C for calculating $wH_2O(S)$, aligning with a previous study that identify this as the onset temperature for structural water release.[54] The mass loss process concludes around 400 °C across all samples. Therefore, we adopted this temperature as the final point for $wH_2O(S)$ calculation. While some studies extend structural water liberation up to 550-600 °C for calculation purposes,[16] assuming a temperature of 400 °C additionally mitigates overestimation of $wH_2O(S)$ by reducing the influence of other thermal events observed at these intermediate temperatures in our TGA/DTG data. These events beyond 400 °C have been associated with intensified CO_3^{2-} thermal decomposition and

Table 1. Chemical composition of carbonated ACP NPs.

$\boldsymbol{Sample}$	$\boldsymbol{wCO_3}$ $(\boldsymbol{wt.\%})^a$	$\boldsymbol{wCO_3}$ $(\boldsymbol{wt.\%})$ $\boldsymbol{after\ HT}^a$	$\boldsymbol{wCa}$ $(\boldsymbol{wt.\%})^b$	$\boldsymbol{wP}$ $(\boldsymbol{wt.\%})^b$	$\boldsymbol{Ca/P}$	$\boldsymbol{wH_2O(S)}$ $(\boldsymbol{wt.\%})^c$
ACP1	0.97	0.62	25.67	13.58	1.46	9.8
ACP2	1.80	1.21	26.73	14.11	1.47	11.2
ACP3	2.65	1.58	26.76	13.73	1.51	10.6
ACP4	4.45	3.28	27.06	13.35	1.57	11.0
ACP5	6.77	5.89	29.41	14.11	1.61	9.5
ACP6	11.11	8.56	26.26	11.74	1.73	11.2
ACP7	17.09	14.00	28.34	11.40	1.92	11.1
ACP8	26.71	23.38	26.24	9.04	2.24	10.7

[a] Determined by FTIR. [b] Determined by ICP-OES. [c] Determined by TGA.

the release of volatile species involved in the crystallization processes of the amorphous structure.[18,20,50]

The results, summarized in Table 1, show that the $wH_2O(S)$ values are closely distributed and range from 9.5 to 11.2 wt.% (average of 10.6 wt.%), with no clear trends observed among the different precipitated samples. These values are in good agreement with those reported by Yasar et al.[19] for carbonated-ACP samples ($wH_2O(S)$ = 9.5-13.3 wt.%, average of 10.8 wt.%), with no evident correlation observed with the extent of carbonation, a trend that aligns with our present findings. In summary, the TGA/DTG results indicate minimized amounts of structural water in the heat-treated NPs and show that the presence of CO_3^{2-} impurities does not significantly impact the structural water content in ACP within the studied range of carbonation degrees.

Structural analysis

The XRD patterns of both the as-synthesized and heat-treated ACP NPs are presented in Figure 1(a,b). In each sample, two broad peaks are observed, at 2θ = 25-35° and 2θ = 40-55°, which are consistent with the typical diffraction pattern of ACP structure.[17] This indicates the absence of long-range order (LRO) in our ACP samples, even with the increased addition of CO_3^{2-} impurity and after the heat treatment at 400 °C. The presence of an ACP single phase in all samples was further confirmed through FTIR analyses. As shown in Figure 1(c,d), the main vibrational modes of PO_4^{3-} groups are observed as broad and unresolved bands between 1300-900 cm^{-1} (ν_1,ν_3PO_4 modes) and between 685-485 cm^{-1} (ν_4PO_4 mode), which are characteristic of ACP structure.[51,55] The doublet between 1560-1330 cm^{-1} and the band at 871 cm^{-1} correspond to the ν_3 and ν_2 vibrational modes of structural CO_3^{2-} groups, respectively.[51] The variations in integrated area of the ν_3 bands reflect the varying degrees of carbonation, as summarized in Table 1. The bands between 3700-2500 cm^{-1} and at 1655 cm^{-1} confirm the presence of adsorbed and structural water molecules in our carbonated ACP samples.[56] The reduction in absorbance of these bands aligns with the TGA analysis, which indicates significant decrease in water content after the heat treatment at 400 °C.

FTIR spectroscopy is also a valuable technique for assessing the degree of short-range order (SRO) in ACP.[49] In this case, the broadening of ν_3PO_4 and ν_4PO_4 bands can be used to monitor changes in SRO, which can be represented by the variations in the FWHM values of these bands.[22,57] No clear trends in the calculated FWHM values within the 128-140 cm^{-1} (ν_3PO_4) and 77-83 cm^{-1} (ν_4PO_4) ranges (Figure S5) were observed among the as-synthesized samples. However, significant changes occurred upon heating the carbonated ACP samples, as depicted in Figure 1(e). The highest FWHM values were observed in ACP2-HT (180 and 87 cm^{-1} for ν_3 and ν_4) and ACP3-HT (175 and 88 cm^{-1} for ν_3 and ν_4), indicating that these samples exhibited the highest degree of disorder at short-range, characterized by increased absorption of various frequencies resulting from fluctuations in P–O bonds length and in the O–P–O bond angles within distorted PO_4 tetrahedra.[22]

Furthermore, the greatest increase in FWHM after the heat treatment at 400 °C, relative to the corresponding as-synthesized sample, was also observed in ACP2-HT and ACP3-HT samples, as determined by the $FWHM_{HT}/FWHM_{Raw}$ ratio shown in Figure 1(f). Notably, the $FWHM_{HT}/FWHM_{Raw}$ values exhibit an increasing trend from 1.25 (ν_3PO_4) and 1.08 (ν_4PO_4)

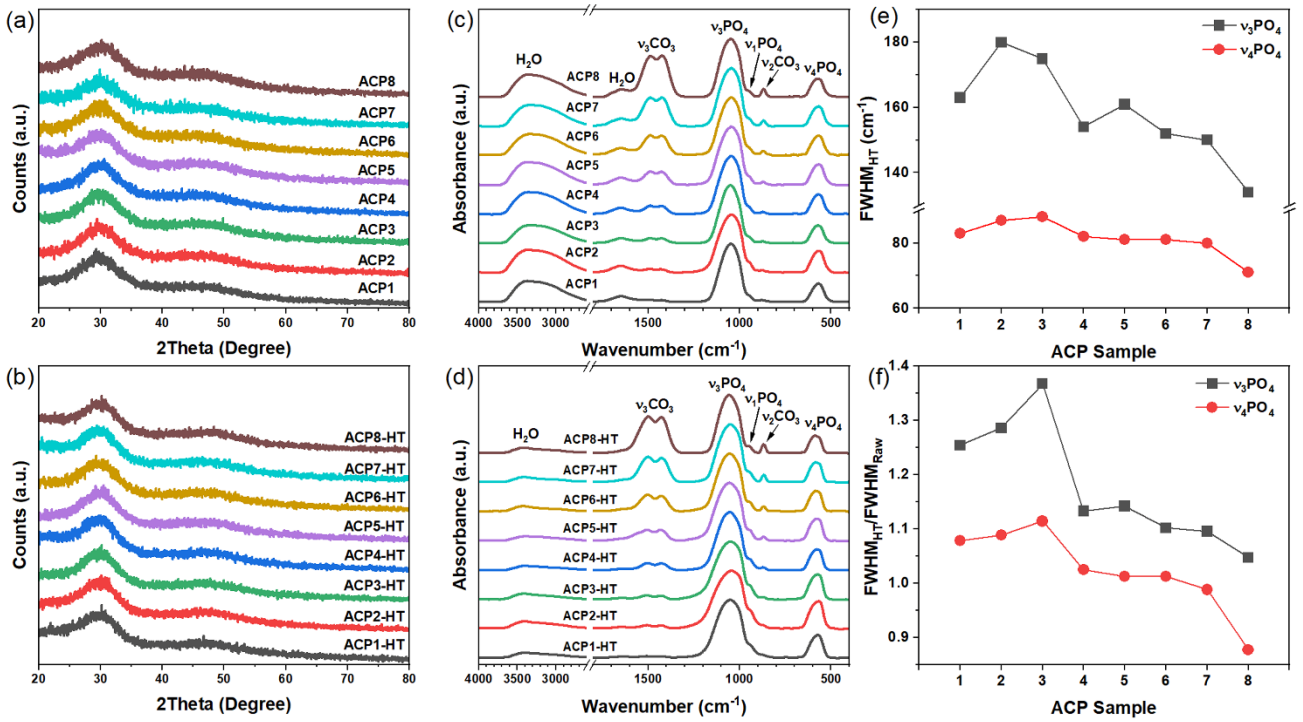

Figure 1. Structural characterization of carbonated-ACP NPs. (a,b) XRD patterns and (c,d) FTIR spectra of as-synthesized and heat-treated samples. (e) FWHM of ν_3,ν_4PO_4 bands calculated from FTIR spectra of heat-treated samples, and (f) $FWHM_{HT}/FWHM_{Raw}$ ratio of ν_3,ν_4PO_4 bands.

in the ACP1-HT sample to 1.37 (ν_3PO_4) and 1.11 (ν_4PO_4) in the ACP3-HT sample. This observation suggests that the heating step had the most substantial structural impact on the ACP3 sample, resulting in a more pronounced disorder at the short-range in ACP3-HT sample. Subsequently, a continuous decline in the $FWHM_{HT}/FWHM_{Raw}$ values occurred, indicating a progressive reduction in the broadening of the ν_3PO_4 and ν_4PO_4 bands due to a diminished effect on SRO caused by the heat treatment. Important features are observed in samples ACP7-HT and ACP8-HT, where the $FWHM_{HT}/FWHM_{Raw}$ ratios are 1.09 and 1.04 for the ν_3PO_4 band, and 0.98 and 0.87 for the ν_4PO_4 band, respectively, demonstrating that the ν_4PO_4 bands are slightly narrower than those of their corresponding as-synthesized samples.

The broadening of PO_4^{3-} bands indicate that the release of structural H_2O and the concentration of CO_3^{2-} may play a significant role in the degree of short-range disorder after the heat treatment at 400 °C. Previous studies conducted by Uskoković[49] and our group[22] on slightly carbonated ACP samples suggested that the broadening of the PO_4^{3-} bands after heating chemically precipitated samples is attributed to the lattice shrinkage, which occurs to eliminate empty spaces left in the ACP structure after loss of structural H_2O. This process increases the lattice stress, similarly to the thermally induced dehydration of $CaCO_3$,[2] resulting in more distorted environments around PO_4^{3-} groups. We can infer that as the concentration of CO_3^{2-} groups increases in slightly carbonated ACP samples (from ACP1-HT to ACP3-HT), the amorphous structure of ACP becomes more susceptible to undergoing an increase in short-range lattice disorder due to the elimination of structural water. However, the opposite trend is observed in samples with higher concentrations of CO_3^{2-} (from ACP4-HT to ACP8-HT). In these cases, the decrease in short-range ordering of PO_4^{3-} groups and their surroundings due to water elimination become progressively less significant, until virtually no impact is detected in ACP7-HT and ACP8-HT samples. Owing to the significant concentration of carbonates in these samples, they could also be regarded as hybrid NPs of amorphous calcium carbonate/phosphate. This suggests a stabilizing effect of CO_3^{2-} groups on the ACP structure at high degrees of carbonation.

On the other hand, the slight decrease in the intensity of the ν_3CO_3 bands, corresponding to partial sublimation as CO_2, was accompanied by noticeable blueshift of the doublet from 1488 and 1423 cm^{-1} to 1501 and 1426 cm^{-1} in all samples. Additionally, the separation between these bands increased from 65 to 75 cm^{-1}. These observations are consistent with our previous findings,[22] indicating a strong interaction between H_2O and CO_3^{2-} groups through hydrogen bonding. The changes in the surroundings of CO_3^{2-}, resulting from the elimination of H_2O molecules, lead to distinct stereo-chemistries for CO_3^{2-} groups with consequent variations in bond energies before and after the heat treatment step.

Photoluminescence properties in solid state

The influence of heat treatment and degree of carbonation on the PL properties of carbonated ACP NPs was investigated. Figure 2(a) shows the emission spectra of the as-synthesized ACP NPs excited at a wavelength of 405 nm. These spectra exhibit similar asymmetric broadband emission with two main emission centers at 440 and 471 nm, corresponding to the blue region of the visible electromagnetic spectrum. Deconvolution analysis, as demonstrated in Figure 2(b) for the ACP3 sample,

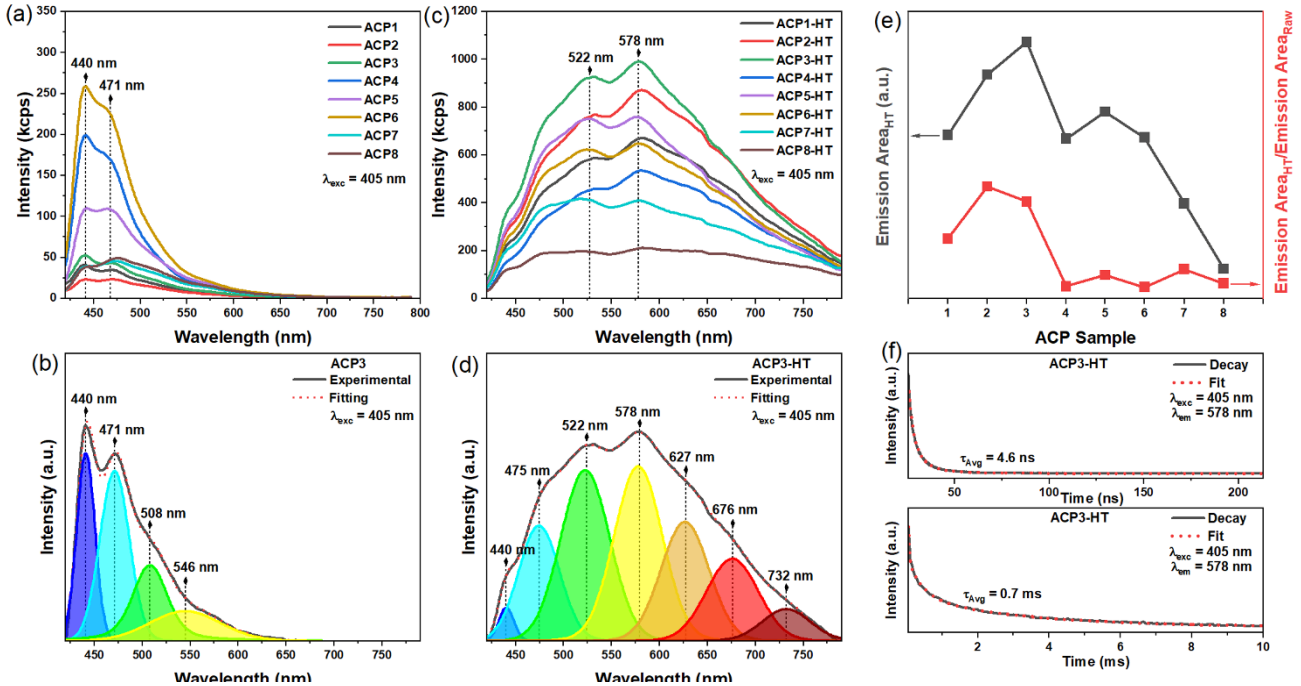

Figure 2. PL properties of carbonated-ACP NPs powders. (a) Emission spectra of as-synthesized NPs, (b) deconvolution of ACP3 emission profile, (c) emission spectra of HT samples, and (d) deconvolution of ACP3-HT emission profile. (e) Emission area of HT samples and ratio between the emission area of HT and as-synthesized samples. (f) Decay curves for the PL of ACP3-HT NPs.

revealed that the emission bands in as-synthesized samples consist of four components centered at 440, 471, 508, and 546 nm. Previous research conducted by our group has shown that the PL properties in ACP are related to lattice disorder.[22] This disorder leads to localized energy states into the forbidden zone of the band structure, facilitating radiative recombination of electron-hole (e^--h^+) pairs. Specifically, when ACP NPs are excited at wavelengths corresponding to energies lower than the band gap energy (Eg ~5.4 eV[22]), such as the excitation wavelength used in our experiment (λ_{exc} = 405 nm, corresponding to 3.1 eV), these localized states enable the self-activated PL.

Given the high structural flexibility of CaPs, various defects could contribute to defect-related energies states within the band gap of ACP NPs, including calcium vacancies (V_{Ca}), and oxygen vacancies (V_O) in PO_4^{3-} groups.[58] Furthermore, localized tail states arising from variations in Ca–O and P–O bonds length and O–Ca–O and O–P–O bonds angle, intrinsic to the amorphous structure or due to defects in their surroundings, can contribute to localized energy-states.[22] The results in Figure 2(a) provide strong evidence that the presence of CO_3^{2-} impurities, substituting PO_4^{3-} groups, has a significant impact on the PL of ACP. Notably, the main effect of CO_3^{2-} is observed in changes in the emission intensity, with the highest emission observed in ACP6 sample, i.e., carbonate groups facilitate radiative transitions until wCO_3 = 11.11 wt.%. This finding suggests that CO_3^{2-} impacts the PL emission probably by acting as a defective emission center within the ACP structure and/or by affecting the balance of other defects in the lattice (V_{Ca} and P_O vacancies). The latter can also occur by the distortions associated to the allocation of CO_3^{2-} with different size compared to PO_4^{3-} groups.

Figure 2(c) displays the PL emission spectra of heat-treated carbonated ACP NPs. A noticeable shift of emission maxima and a broadening of the emission profile are observed compared to the spectra of as-synthesized samples. Specifically, the emission maxima are now centered at 522 and 578 nm, corresponding to the green/yellow regions of the electromagnetic spectrum. Moreover, the emission spectra now range from 420 to 800 nm, encompassing the entire visible spectrum, in contrast to the range of 420 to 650 nm observed in as-synthesized samples. The broadening of the profile is attributed to the emergence of new emission components following the heating step, as demonstrated by the deconvoluted spectrum of ACP3-HT sample depicted in Figure 2(d). In the heat-treated samples, seven distinct emission components are present at 440, 475, 522, 578, 627, 676, and 732 nm, exceeding the four components in the as-synthesized samples.

PL spectroscopy is a sensitive technique that can detect variations in lattice order-disorder at short-range in materials.[59] In the case of heat-treated carbonated ACP NPs, both the broadening and red shift of the emission profile indicate an increase in short-range disorder within the material, and this increase in disorder leads to the occurrence of new energy states within the band gap. This result is consistent with the observed changes in lattice ordering identified in the FTIR spectroscopy. Based on the literature, the higher density of localized states with varying energies for the radiative recombination of charge carriers in heat-treated samples can be attributed to several factors, namely: (i) The shrinkage of the structure during the heat treatment process, which leads to an increase in lattice strain as the voids formed by water elimination are closed[49], (ii) distortions in the strong polarizable PO_4^{3-} and CO_3^{2-} groups after the removal of water molecules, as a result of the close $PO_4^{3-}\cdots H_2O$ and $CO_3^{2-}\cdots H_2O$ interactions,[19] (iii) an increase in the concentration of V_O vacancies, which has been associated to the heat treatment step in carbonated-HA[60,61], (iv) higher density of recombination of self-trapped electrons (CO_3^{3-}) and holes in excited CO_3^{2-} groups.[32] Furthermore, structural water can act as traps for charges (electrons or holes) and serve as centers for nonradiative recombination for charge carriers. By providing alternative relaxation pathways for e^--h^+ pairs, water molecules can effectively quench the PL emission.[62] Therefore, the elimination of structural water potentially reduces the presence of quenching centers that impede radiative recombination pathways of e^--h^+ pairs.

Similar to the as-synthesized samples, the extent of carbonation plays a significant role in the magnitude of PL emissions of heat-treated samples (Figure 2(c)), providing further evidence of the correlation between CO_3^{2-} groups and self-activated PL in carbonated ACP NPs. To better illustrate this effect, we compared the integrated emission areas between 420 and 800 nm, as shown in Figure 2(e). Initially, the integrated emission area of the heat-treated samples shows a substantial increase from ACP1-HT to ACP3-HT and then gradually decreases until reaching sample ACP8-HT. This trend corresponds to the changes in structural ordering observed via FTIR spectroscopy. More specifically, the PL emission tends to intensify at lower degrees of carbonation, where an increase in lattice disorder occurs. Conversely, a decrease in emission is observed at higher concentrations of CO_3^{2-} groups, which stabilize ACP structure and result in a lesser increase in lattice disorder through the heat treatment step. This finding is further supported by the ratios between the integrated emission area of heat-treated and as-synthesized (raw) samples, as shown in Figure 2(e), which are significantly higher for samples ACP1-HT to ACP3-HT.

Therefore, it can be inferred that the heat treatment step has a more pronounced impact on the PL magnitude of ACP samples with a low degree of carbonation, possibly due to its stronger influence on SRO. Complementary, it is important to consider that other effects could occur simultaneously. In samples with lower concentrations of luminescent centers, such as CO_3^{2-} and associated defects in ACP1-HT to ACP3-HT, there is a predominance of radiative recombination. However, as the concentration of these centers increases until reaching sample ACP8-HT, nonradiative pathways, including energy transfer, trapping, or quenching, could become more prevalent.

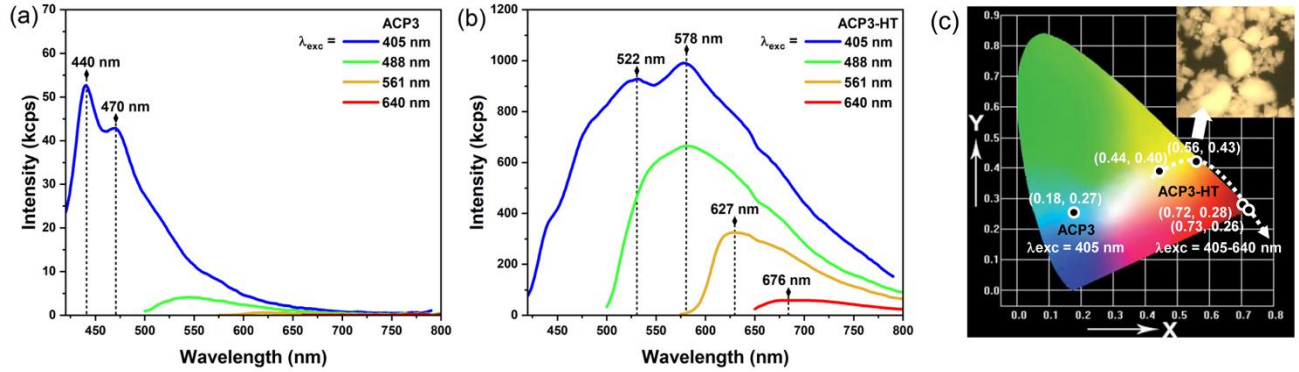

Figure 3. Excitation-dependent emission spectra of: (a) ACP3, and (b) ACP3-HT NPs. (c) CIE chromaticity diagram for ACP3 and ACP3-HT NPs.

The luminescence decay curves for ACP3-HT in solid state reveal the variable nature of the emission of these samples. The decay profiles of ACP3-HT are shown in Figure 2(f). Faster events observed in the first 200 ns of decay must be related to defects in the ACP structure, which can be confirmed by the short average τ value, 4.6 ns, typical for the luminescence caused by defects. On the other hand, slower components are assigned to the recombination of defects between energy levels within the band gap. When ACP NPs are excited at wavelengths that have energies below the band gap energy, such as the excitation wavelength we employed in our experiment, the electron undergoes migration between states of among adjacent crystals until it finds a hole. This leads to radiative recombination within the band gap energy, resulting in an extended τ of 0.7 ms.

The quantum yield of the PL emission for ACP3-HT is 4%, a value that corroborates with the high density of defects within the material. These defects contribute to non-radiative recombination pathways, competing with radiative recombination. Currently, there are no comparisons available in existing literature regarding defect-related luminescent ACP. Only quantum yields ranging from 22% to 74% have been reported for defect-related luminescent HA.[14,63,64] However, it is important to note that these quantum yields are primarily attributed to carbon dots acting as luminescent centers rather than solely originating from the calcium phosphate material itself.[11,63,65]

We investigated the excitation-dependent PL emission of carbonated ACP NPs in comparison to their as-synthesized counterparts. Figure 3(a,b) presents the results from the excitation of ACP3 and ACP3-HT NPs at various wavelengths (λ_{exc} = 405, 488, 561, and 640 nm), which are commonly used in techniques such as flow cytometry and confocal laser scanning microscopy (CLSM). As illustrated in Figure 3(a), the as-synthesized ACP3 sample exhibits minimal PL emission when the excitation wavelength increases. Conversely, ACP3-HT NPs demonstrate prominent PL emission under the probed conditions (Figure 3(b)), with emission maxima at 522 and 578 nm (λ_{exc} = 405 nm), 578 nm (λ_{exc} = 488 nm), 627 nm (λ_{exc} = 561 nm), and 676 nm (λ_{exc} = 640 nm). The latter agrees with the higher density of localized acceptor/donor energy levels within the band gap compared to the as-synthesized sample. The excitation spectra illustrated in Figure S6 for both samples also support the increased presence of optically active localized states within the bandgap for the ACP3-HT sample. Figure S7 shows a comparison between ACP3 and ACP3-HT emission spectra, highlighting the considerably higher emission intensity observed in ACP3-HT in all excitation wavelengths. Both the as-synthesized and heat-treated samples exhibit similar excitation-dependent behavior within each group, with variations only in emission intensities (Figure S8).

The color of emission in the ACP3-HT sample is influenced by the elimination of radiative emissions at shorter wavelengths as the excitation wavelength increases. As shown in the Comission Internationale de l'Éclairage (CIE) chromaticity diagram (Figure 3(c)), the CIE coordinates are (0.44, 0.40) for λ_{exc} = 405 nm, (0.56, 0.43) for λ_{exc} = 488 nm, (0.72, 0.28) for λ_{exc} = 561 nm, and (0.73, 0.26) for λ_{exc} = 640 nm, corresponding to yellow, orange (inset, Figure 3(c)), and red emission, respectively.

Our studies showcase the effectiveness of employing a heat treatment step following the precipitation procedure, along with an optimized concentration of CO_3^{2-} impurity, to enhance the PL properties of carbonated ACP NPs by manipulating the density and nature of defects. Despite the low quantum yield observed in defect-related luminescent ACP NPs presents a current challenge for some applications, these NPs potentially offer other several advantages. These include biocompatibility, biodegradability, and photostability, minimizing concerns about signal degradation and potential photodamage in biological samples.[66] Moreover, their straightforward synthesis, cost-effectiveness, and amenability to surface functionalization serve to counterbalance the low luminescence. Thus, their use remains appealing for various bioimaging applications where the benefits of their unique properties outweigh their inherent drawbacks.

Citrate functionalization

NPs are often used in suspension for various nanomedicine applications. However, it is well-established that unmodified CaP NPs tend to aggregate, limiting their applicability due to potential cytotoxic effects and other adverse outcomes.[4] To address this issue, we employed citrate ions to functionalize our

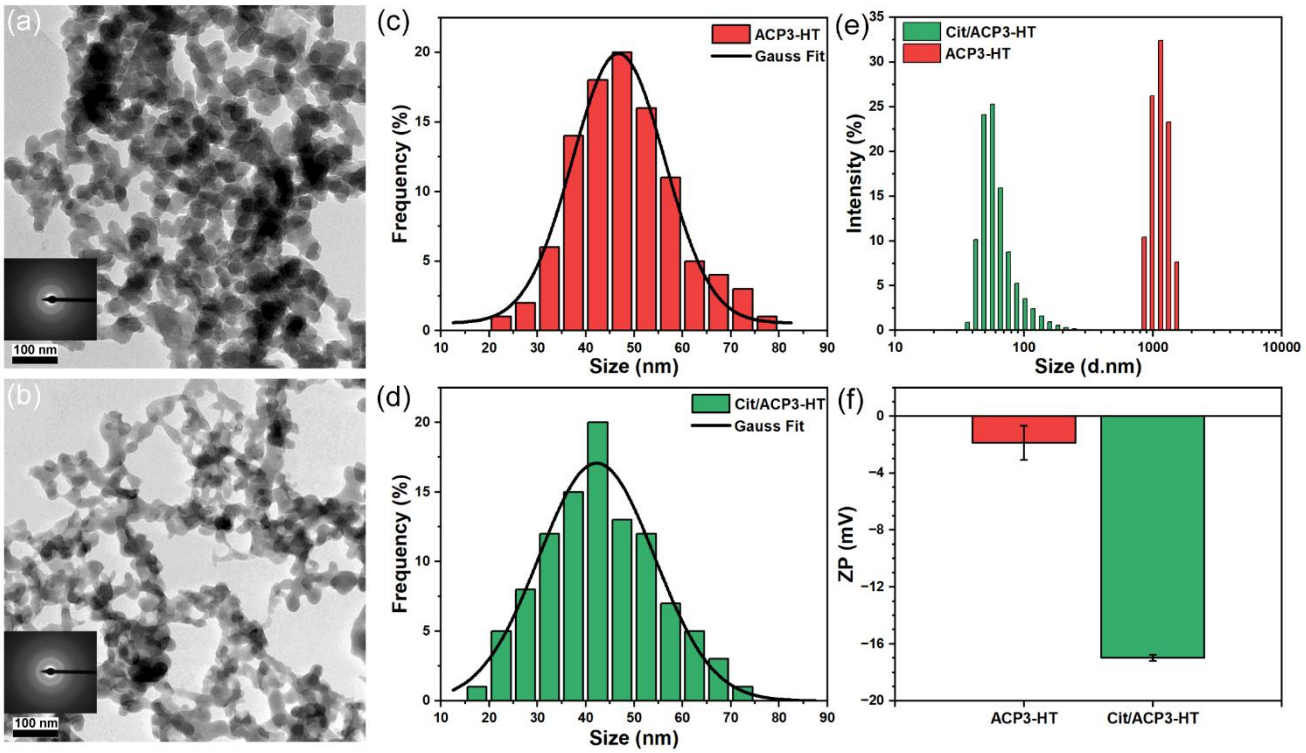

Figure 4. (a,b) TEM micrographs and (c,d) calculated size distribution of ACP3-HT and Cit/ACP3-HT NPs, respectively. (e) Size distributions obtained via DLS characterization and (f) ZP values for both NPs in water (pH 10).

luminescent NPs. Citrate ions are widely recognized for their high biocompatibility and their ability to enhance the colloidal stability of CaPs.[9,40] ACP3-HT NPs was chosen due to their optimized PL properties. The successful functionalization of ACP3-HT samples with citrate was confirmed through FTIR analysis, where the vibrational bands at approximately 2930 and 1590 cm^{-1} corresponding to the νCH_2 and δCOO modes of citrate[43] were observed in the spectrum of Cit/ACP3-HT NPs (refer to Figure S9). The amount of citrate adsorbed per milligram of NPs was determined using UV-Vis, yielding a value of 191.9 ± 21.3 $\mu g.mg^{-1}$, a substantial amount comparable to that reported by Kataoka et al.[67] for Eu^{3+}-doped HA NPs (157-189 $\mu g.mg^{-1}$).

Figure 4(a,b) shows TEM micrographs of ACP3-HT and Cit/ACP3-HT samples. Both samples consist of irregular rounded-shaped NPs, with the Cit/ACP3-HT NPs forming the typical chain-like structure[68] in a more dispersed manner. SAED analysis revealed that incorporation of citrate ions did not induce any chances on ACP phase, as the diffraction pattern was preserved after functionalization. The NPs sizes were found to be similar in both samples, ranging from 20 to 80 nm, as evidenced by the size distribution estimations shown in Figure 4(c,d). Table 2 provides the calculated mean particle sizes of 46.7 ± 0.4 nm for ACP3-HT and 42.2 ± 0.6 nm for Cit/ACP3-HT samples.

The differences between ACP3-HT and Cit/ACP3-HT suspensions are evident in the DLS characterization, as depicted by the size distribution plot in Figure 4(e) and the corresponding mean particle sizes and PDI values listed in Table 2. The ACP3-HT NPs observed by TEM display a wide range of sizes in the DLS analysis, with a mean size of 1374 ± 451.7 nm and PDI of 0.890 ± 0.191. These results indicate that the ACP3-HT NPs are unstable in solution and prone to form large agglomerates. In contrast, the functionalization of NPs with citrate ions leads to reduced size distribution and polydispersity. The Cit/ACP3-HT sample exhibit a mean size of 69.1 ± 14.3 nm and PDI of 0.391 ± 0.095, which is closer to the sizes observed by TEM for individual particles. These findings confirm that citrate-stabilized suspensions of ACP NPs possess the desirable particle sizes for the intended applications in this study.

Table 1. Mean sizes estimated by TEM and DLS for ACP3-HT NPs before and after functionalization with citrate ions.

Parameter	ACP3-HT		Cit/ACP3-HT	
	TEM	DLS	TEM	DLS
Mean size (nm)	46.7 ± 0.4	1374 ± 451.7	42.2 ± 0.6	69.1 ± 14.3
PDI	-	0.890 ± 0.191	-	0.391 ± 0.095

The surface charge of ACP3-HT and Cit/ACP3-HT NPs was assessed using ZP measurements (Figure 4(f)). The ZP values in water (pH 10) changed from -1.88 ± 1.21 mV in the ACP3-HT sample to -17.0 ± 0.22 mV in the Cit/ACP3-HT sample, indicating a shift from near-neutral to negatively charged NPs after the functionalization with citrate ions. The carboxylate groups (COO^-) derived from citrates strongly interact with Ca^{2+} on the surface of ACP NPs, allowing their attachment, and the additional negative charge can be attributed to COO^- groups

that remain unbound to the ACP surface.[40,43] As the pH of the solution decreases from 10 to 3, the ZP becomes less negative (Figure S10), reaching -4.7 ± 0.75 mV at pH 3 due to the increased protonation of free COO^- groups on the surface of Cit/ACP3-HT NPs. The observed values across the pH range are close-related to those reported for biomimetic citrate-adsorbed carbonated HA.[43,69] Moreover, the ZP of our NPs at pH 7.4, representative of blood circulation, measures -9.0 ± 0.39 mV, a result consistent with values reported by Chen et al.[40] and Chatzipanagis et al.[41], which are -11.7 ± 0.39 mV and -10.5 ± 3.9 mV, respectively. At pH 5.0, corresponding to the endosomal compartments, the ZP of Cit/ACP3-HT NPs is -6.1 mV ± 0.14 mV.

It is widely recognized that highly cationic NPs are swiftly eliminated from circulation to a greater extent than highly anionic NPs, whereas neutral or slightly negatively charged NPs, such as our Cit/ACP3-HT NPs, exhibit prolonged circulating half-lives, further enhancing the accumulation in tumors.[70] Additionally, we have confirmed the stability of Cit/ACP3-HT NPs over 24 h (see Figure S11), a period during which the majority of the NPs are internalized by cells (see Figure 8), potentially enabling their visualization via PL within cellular environments.

Amorphous phase stability

The metastable nature of ACP phases and their tendency to spontaneously crystallize into HA phase upon exposure to aqueous environments is a crucial consideration for their applications in nanomedicine. In addition to evaluating colloidal stability, it is important to investigate the stability of the amorphous phase over time. Figure 5(a) shows the FTIR spectra collected from aliquots of unfunctionalized ACP3-HT NPs suspended in H_2O from 2 h to 8 h. The spectra remained almost unchanged for at least 7 h in H_2O, with characteristic broadbands of ACP structures observed at ~1050 cm^{-1} (ν_3PO_4) and ~572 cm^{-1} (ν_4PO_4).[51] At 8 h, sharp and resolved bands emerged at 1110 and 1027 cm^{-1} (ν_3PO_4), as well as at 604 and 565 cm^{-1} (ν_4PO_4), indicating the formation of poorly crystalline HA.[71] However, through a refined analysis utilizing the second derivative of the ν_3PO_4 bands region (see Figure S12), the components attributed to the HA phase begin to appear at 7 h of incubation, coexisting with the ACP components. The stability of the amorphous phase of our NPs slightly surpasses those identified by Somrani et al.[72], who observed a significant conversion of a slightly carbonated-ACP sample heat-treated at 400 °C after 5 h of immersion in water. These authors concluded that elimination of structural water in heat-treated ACP enhances the stability of the amorphous phase compared to as-synthesized ACP, which beings to convert into HA in just ~1 h.[72]

The functionalization of citrate ions onto the surface of the NPs leads to a significant increase in the stability of the amorphous phase for an extended period of at least 96 h in water. This is evident from the presence of broad and unresolved ν_3,ν_4PO_4 bands in all the FTIR spectra presented in Figure 5(b), which were collected over time from aliquots of the Cit/ACP3-HT sample. Chatzipanagis et al.[41] attributed this stabilization effect to the adsorption of citrate onto ACP, which

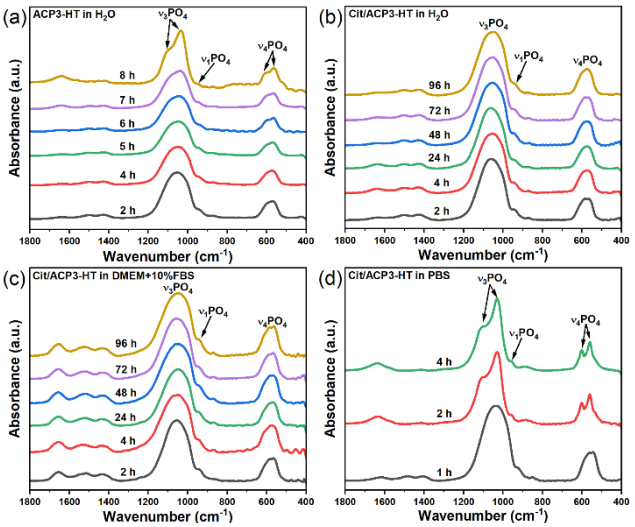

Figure 5. Amorphous phase stability over time of unfunctionalized and citrate-functionalized ACP3-HT NPs. (a) FTIR spectra of ACP3-HT dispersed in H_2O, (b) FTIR spectra of Cit/ACP3-HT dispersed in H_2O, (c) FTIR spectra of Cit/ACP3-HT dispersed in DMEM+10%FBS (pH 7.4, T = 37 °C), and (d) FTIR spectra of Cit/ACP3-HT dispersed in PBS buffer (pH = 7.4).

blocks active sites on the NP surfaces and delays the hydrolysis of ACP in aqueous media, thereby impeding its crystallization into HA. However, their *in situ* RAMAN measurements revealed that the conversion of ACP to HA begins at 14 h in ultrapure water and is completed at 54 h for chemically precipitated ACP NPs in the presence of citrate ions.[41] The higher stability observed in our Cit/ACP3-HT sample can be attributed to a combination of factors, including the presence of CO_3^{2-} groups[73] and the elimination of structural water through heat treatment.[72] These factors collectively contribute to the stabilization of the amorphous structure, in addition to the adsorbed citrate ions.

Similar to the results obtained in water, the Cit/ACP3-HT NPs dispersed at 37 °C in the culture medium (DMEM+10% FBS) used in the *in vitro* assays showed no detectable crystallization events over the examined period of 96 h, as depicted in Figure 5(c). The bands observed in 1700-1400 cm^{-1} range are associated to protein adsorption from FBS.[74] On the other hand, rapid crystallization occurred when the NPs were exposed to PBS solution, with the characteristic bands of HA appearing in the FTIR spectra after only 2 h, as shown in Figure 5(d) and supported by the second derivative analysis (see Figure S13). This behavior is well-documented and attributed to the exchange between adsorbed citrate and phosphate groups in the solution, which accelerates the crystallization of HA.[41] Therefore, the prepared Cit/ACP3-HT NPs exhibit stability for adequate periods in water and culture medium, making them suitable for the intended applications. However, it is important to avoid long-term exposure to PBS buffer solution to preserve the structural integrity of the NPs.

Photoluminescence in liquid

Several factors in solution can influence the PL of NPs. Figure 6(a,b) shows the PL emission of ACP3-HT and Cit/ACP3-HT NPs

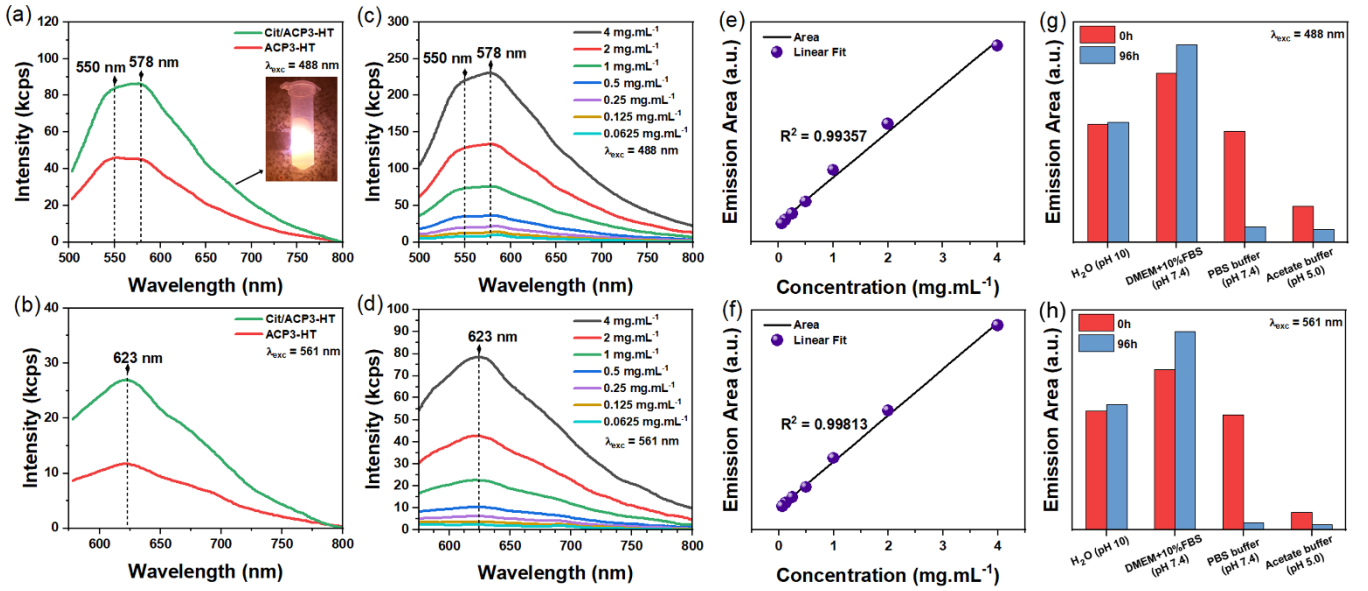

Figure 6. PL properties of Cit/ACP3-HT NPs dispersed in H_2O. (a,b) PL emission spectra of ACP3-HT and Cit/ACP3-HT NPs at 1 mg.mL^{-1}, (c,d) Cit/ACP3-HT emission spectra recorded at distinct NPs concentration, (e,f) linear plots relative to the integrated emission areas at distinct concentrations for λ_{exc} = 488 and 561 nm, and (g,h) integrated emission area of Cit/ACP3-HT NPs dispersed in distinct aqueous media at 1 mg.mL^{-1}.

suspended in water (pH 10) at λ_{exc} = 488 and 561 nm, respectively. The profiles resemble those observed in powder characterization, with emission bands centered at 550/578 (λ_{exc} = 488 nm) and 623 nm (λ_{exc} = 561 nm). Notably, citrate functionalization induces a significant increase in emission intensity, evident in the integrated emission areas of ACP3-HT and Cit/ACP3-HT samples (Figure S14). Surface phenomena substantially contribute to the PL properties of citrate-functionalized CaPs NPs, as observed by Kataoka et al.[75], who found similar behavior in Eu^{3+} luminescence in doped HA NPs. They attributed the increase in PL intensity to citrate-complex formation with surface cationic species like Ca^{2+} and Eu^{3+}, thereby inhibiting non-radiative deactivation processes on the NP surface.[75] Therefore, our results suggest that active bonding of citrates with Ca^{2+} on Cit/ACP3-HT NPs surfaces potentially shield them from the influence of external agents (such as OH groups of water molecules) that negatively affect their PL properties, while also mitigating surface defects that lead to non-radiative recombination pathways of charge carriers. Moreover, the increased dispersion of the NPs resulting from the citrate functionalization can also contribute to enhancing the PL emission. It's noteworthy that the observed behavior differs from that reported by Zhang et al.[64,76], where self-activated luminescence in HA was attributed to $CO_2^{\bullet-}$ radical impurities resulting from citrate cleavage during hydrothermal treatment. Subsequent studies identified these impurities as carbon dots,[11,65] further distinguishing the underlying mechanisms.

Understanding the concentration-dependent effects is necessary for optimizing and evaluating the performance of the luminescent NPs suspensions. In our study, we dispersed the Cit/ACP3-HT in H_2O at various concentrations ranging from 0.0625 to 4 mg.mL^{-1}, as illustrated in Figure 6(c,d) for excitation wavelengths of 488 and 561 nm, respectively. A gradual increase in emission intensities is observed, and the calculated integrated emission area demonstrates a linear dependence on the NPs concentrations, as shown in Figure 6(e,f). These results indicate the absence of artefacts and suggest a reduced probability of particle-particle interactions, thereby minimizing energy transfer, quenching effects, and reabsorption of emitted photons by neighboring NPs within the probed concentration range. Additionally, the functionalization of NPs with citrate successfully prevents saturation effect at higher concentrations, associated with NPs aggregation.

The emission spectra of Cit/ACP3-HT were also obtained by dispersing them in various aqueous environments with varying pH levels, as shown in the t = 0 h measurements of Figure S15. The integrated emission area was then calculated, as depicted in Figure 6(g,h). In both water (pH 10) and PBS buffer (pH 7.4), the PL profile and emission area exhibit remarkable similarity. However, in DMEM+10%FBS (pH 7.4), while the profile remains similar, there is a notable increase in emission area, potentially due to adsorbed proteins enhancing the mitigation effect against non-radiative deactivation of PL. Conversely, in acetate buffer (pH 5.0), the emission significantly diminishes, accompanied by a blueshift of the emission band, likely attributable to the recognized dissolution of CaPs in acidic conditions.[5,21,43]

Upon extending the exposure time to 96 h, the emission profile maintains similarity in water, with a slight intensity increase observed in DMEM+10%FBS compared to t = 0 h, possibly due to a more stable protein conformation on the NPs surfaces. However, in PBS buffer, the emission becomes almost negligible, a decrease that becomes noticeable even after 4 h of contact (Figure S16). This trend was also observed in unfunctionalized ACP3-HT NPs (Figure S17). As previously described in our recent studies,[22] this decrease is linked to the conversion of the amorphous ACP phase to poorly crystalline HA phase, which suppresses the main defects responsible for PL originated in ACP structure due to the heat treatment step.

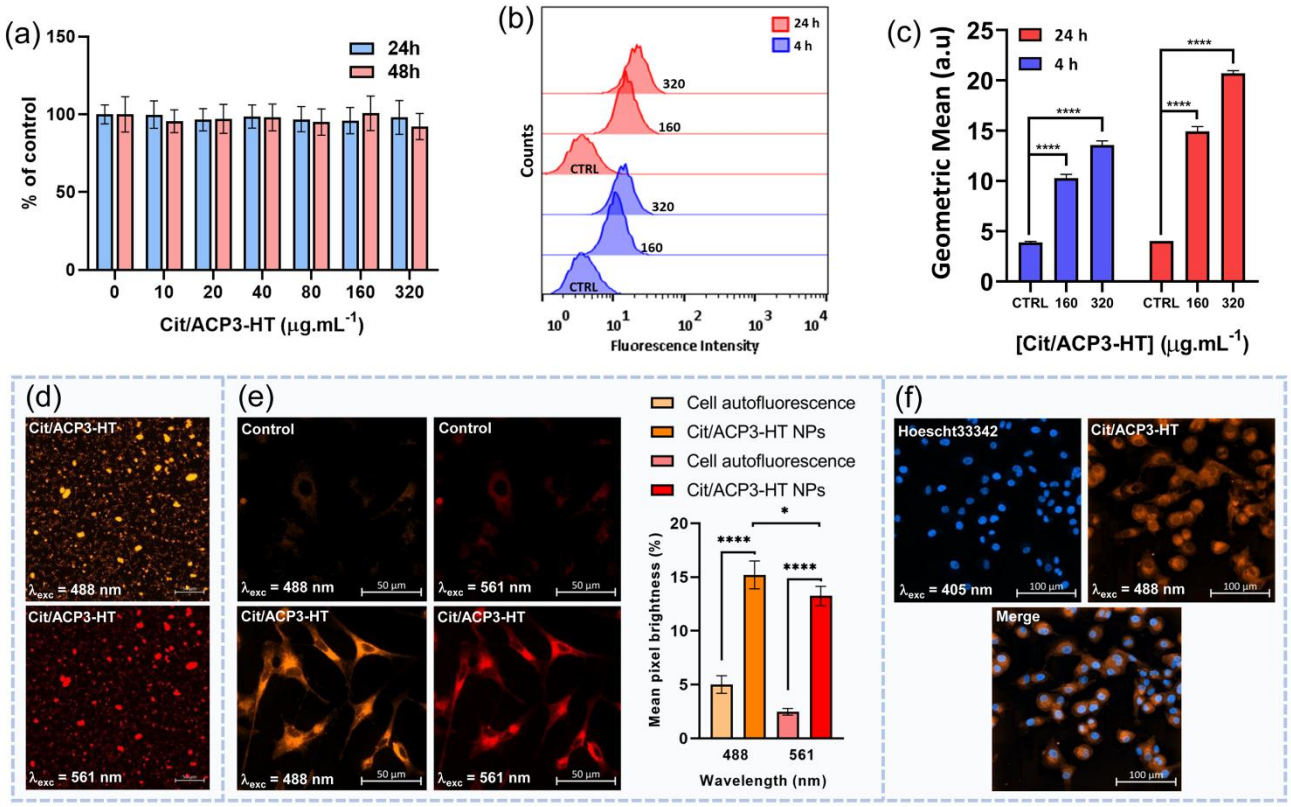

Figure 7. (a) Cell viability via MTT assay of HepaRG cells after incubation for 24 and 48 h with different concentrations of Cit/ACP3-HT NPs ranging from 10 to 320 μg.mL^{-1}, (b) flow cytometric analysis of HepaRG cells incubated with blank solution and Cit/ACP3-HT NPs at 160 and 320 μg.mL^{-1} for 4 and 24 h, (c) quantification of the mean fluorescence intensities (geometric mean) for the HepaRG cell lines. Significance at the levels of *, $p < 0.05$; **, $p < 0.01$; ***, $p < 0.001$; and ****, $p < 0.0001$ was determined using One-way ANOVA and Tukey's test, (d) CSLM images of Cit/ACP3-HT powders using a 20x objective lens, (e) CSLM of blank HepaRG cells (control) and co-incubated with Cit/ACP3-HT NPs at 320 μg.mL^{-1} for 24 h using a 40x oil immersion objective lens, PL quantification using image processing analysis based on the mean pixel brightness of the CLSM images (n=4), and (f) CLSM images of HepaRG cells co-incubated with Cit/ACP3-HT NPs at 160 μg.mL^{-1} for 4 h (orange) and labeled with Hoescht33342 (blue) using a 20x objective lens.

After 96 h, the emission in acetate buffer adopts a shape and intensity similar to that of PBS buffer at the same time, likely due to increased NPs dissolution over time at the acidic conditions. Finally, a slight decrease in PL intensity is sensed in terms of increase of ionic strength (Figure S18).

In summary, the Cit/ACP3-HT NPs exhibited stable PL emission in H_2O (pH 10) in distinct concentrations and under simulated physiological conditions with DMEM+10%FBS (pH 7.4). However, significant decrease in PL intensity was observed in PBS buffer (pH 7.4) and acetate buffer (pH 5.0). These PL results suggest potential applications, respectively, as an easy and accessible technique for monitoring ACP→HA phase transition and as pH-responsive nanocarriers and bioimaging agents to monitor intracellular events, the latter of which has already been explored in the case of self-activated luminescent HA NPs.[77] The variation in PL intensity with ionic strength remains a challenge for the desired applications but it endows the possibility for exploring the NPs for ions detection.

Cytotoxicity assay, flow cytometry and confocal microscopy

In the present study, we conducted the MTT assay to assess the cytotoxicity of the Cit/ACP3HT NPs at different particles concentrations ranging from 10 to 320 μg.mL^{-1}. HepaRG cells were incubated with the NPs for 24 and 48 h for this analysis. Figure 7(a) shows the cell viability results compared to the control group. There were no statistically significant variations in viability values across all tested conditions, indicating the absence of cytotoxic effects from the Cit/ACP3-HT NPs. These findings agree with the literature that highlights the high biocompatibility of calcium orthophosphates.[66] Consequently, these self-activated photoluminescent, citrate-functionalized, carbonated-ACP NPs exhibit significant potential as a biocompatible nanosystem for applications in nanomedicine.

The internalization of NPs into cells is a fundamental process that underlies their potential applications. Flow cytometry serve as a valuable tool for evaluating the uptake of NPs within a cell population by assessing the PL signal emitted by the NPs. In this study, our objective was to investigate the cellular uptake of Cit/ACP3-HT NPs using flow cytometry and assess the suitability of their self-activated PL emission for this technique. Figure 7(b) shows the results of PL intensity at λ_{exc} = 488 nm, when incubating the NPs with HepaRG cells at concentrations of 160 and 320 μg.mL^{-1} for 4 and 24 h. By analyzing the average PL intensity by terms of geometric mean (Figure 7(c)), we observed statistically significant differences between the control group and all probed groups. These findings indicated that cellular uptake of the NPs is both time and concentration dependent. Notably, a significant internalization occurs after 4 h of incubation, which further increased after 24 h for both concentrations tested, but the NPs at a concentration of 320

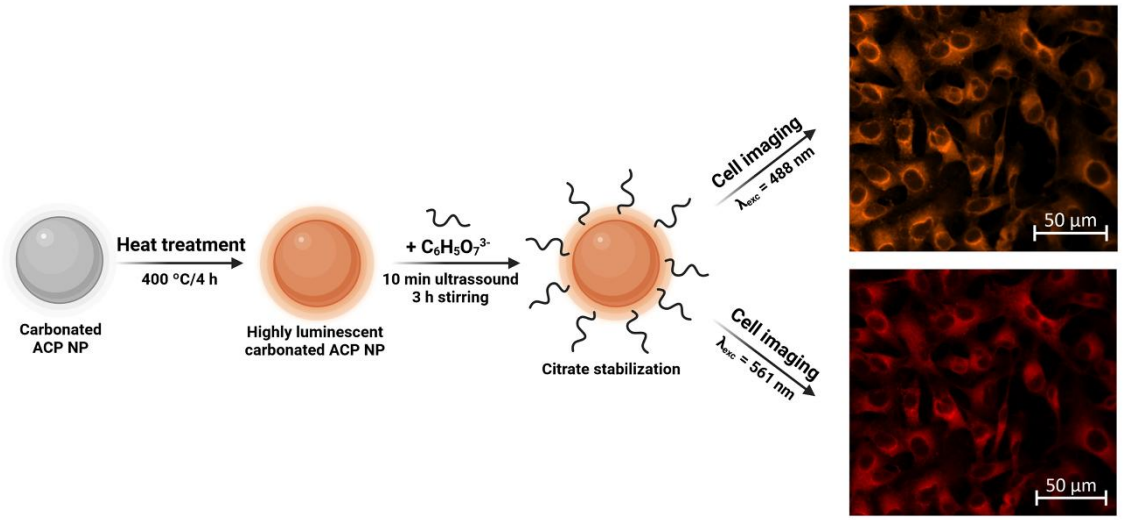

Figure 8. Synthesis methodology of luminescent carbonated ACP NPs with further citrate functionalization for bioimaging purposes.

µg.mL^{-1} exhibited a higher uptake compare to 160 µg.mL^{-1} at both time periods.

The specific mechanism through which CaP NPs internalize into cells are influenced by several factors, including cell type, particles size, shape, charge, coating molecules.[21] While the precise pathways of internalization are still an area of ongoing research, it is generally accepted that endocytic uptake pathways play a major role.[5] It is important to note that the internalization of ACP NPs may be underestimated via PL, particularly after 24 h of incubation, due to the well-known pH-responsive properties of ACP as evidenced in PL measurements shown in Figure S15 and Figure 6(g,h). In acidic environments within endosomes, ACP can undergo partial degradation, resulting in the release of Ca^{2+} and PO_4^{3-} ions during the maturation of endosomes into lysosomes.[21] However, our study demonstrates that Cit/ACP-3HT NPs are readily internalized by cells and exhibit a sufficiently strong PL intensity that allows for analysis by flow cytometry. Furthermore, we anticipate that the self-activated PL emission of carbonated ACP NPs could be leveraged in future investigations, such as monitoring the endosomal escape of pH-responsive drug delivery systems and related studies.

To assess the suitability of Cit/ACP3-HT NPs for bioimaging, we initially performed CLSM imaging of the NPs in powder form, as depicted in Figure 7(d). The CLSM images reveal successful detection of the NPs, displaying pronounced emission intensity represented by the orange and red colors for λ_{exc} = 488 and 561 nm, respectively. This observation underscores the strong and discernible PL emitted by the NPs. Subsequently, we conducted *in vitro* cell imaging experiments using HepaRG cells. The results for cells co-incubating with Cit/ACP3-HT NPs at a concentration of 320 µg.mL^{-1} for 24 h are presented in Figure 7(e). Remarkably, the NPs display intense signal within the cellular interior when excited at both 488 and 561 nm, as represented by the orange and red colors, respectively. The PL departing from the NPs exhibit significantly greater intensity and a more widespread distribution within the cells compared to the autofluorescence observed in the control group lacking NPs. This distinction was further supported by image processing analysis, evaluating the mean pixel brightness of the images and correlating to the PL, which revealed a significant difference ($P < 0.0001$) between the autofluorescence of the cells and the nanoparticles' PL. While there is a significant difference in the light emission of the NPs in both excitation wavelengths ($P<0.05$). These results confirm that the self-activated PL of internalized Cit/ACP3-HT NPs allow intracellular imaging experiments. Moreover, the inherent fusiform shape of the cells remains preserved in the presence of the NPs, thereby reinforcing their excellent biocompatibility.

The findings depicted in Figure 7(f) provide further evidence that Cit/ACP3-HT NPs can be imaged within HepaRG cells even at the lower concentrations (160 µg.mL^{-1}) and incubation times (4 h), which supports the earlier observation of rapid NPs internalization as determined by flow cytometry. Furthermore, despite the broad excitation/emission features of the NPs, our results show that it is feasible to concurrently employ them with commonly used fluorophores such as the Hoescht33342 nucleus marker by appropriately configuring measurement parameters and selecting distinct spectral regions for data collection. Notably, when the NPs are excited at 488 nm, specific labelling of cellular structures is achieved with minimal interference between the different contrast agents. These results validate the potential of the developed self-activated photoluminescent carbonated ACP NPs for fluorescence bioimaging applications.

Figure 8 illustrates the main findings outlined in this study. ACP NPs with tailored carbonate content were produced through a simple chemical precipitation at room temperature, followed by a 400 °C heat treatment. This dual-factor approach (CO_3^{2-} impurity and heat treatment) significantly amplified the self-activated PL properties of the NPs. Subsequently, the NPs were stabilized through citrate ions functionalized onto the ACP surface. These optimized NPs effectively enabled cell imaging using excitation wavelengths of 488 and 561 nm, relying on defect-related PL without the necessity of additional luminescent centers.

Conclusions

Carbonated ACP NPs were synthesized through chemical precipitation, using various $[CO_3]/[PO_4]$ molar ratios ranging from 0.0625 to 4. The synthesized carbonated ACP samples underwent a heat treatment at 400 °C for 4 h, preserving the amorphous structure of ACP, but inducing changes in short-range ordering mainly associated with the release of structural water, which significantly enhance the photoluminescent properties of carbonated ACP NPs. Our findings reveal that the precise combination of an appropriate amount of carbonate groups ($[CO_3]/[PO_4]$ = 0.125, corresponding to 1.58 wt.% of carbonates) and the heat treatment leads to the optimization of multicolor excitation-dependent PL emission in carbonated ACP.

The heat-treated ACP sample containing 1.58 wt.% of carbonates was successfully functionalized with citrate ions. These ions played a crucial role in stabilizing the suspensions in solution, as well as in preventing their crystallization into calcium-deficient carbonated HA, and in maintaining stable PL emission for at least 96 h in both H_2O (pH 10) and DMEM+10%FBS (pH 7.4). Additionally, citrate functionalization enhanced PL intensity by protecting against quenching agents in aqueous environments or non-radiative recombination pathways of charge carriers. The PL properties also revealed prospects for monitoring both the crystallization process in PBS (pH 7.4) and pH-responsive behavior in acidic environments (pH 5.0). The PL intensity showed slight variations with increasing ionic strength of the Tris-HCl solution (pH 7.4, 100-200 mM).

MTT analysis with Hepa-RG cells showed no interference in cell viability for citrate-functionalized NPs at concentrations between 10–320 $ug.mL^{-1}$ incubated for 24 or 48 h. Finally, the self-activated PL of the NPs allowed to determine their internalization behavior within cells via flow cytometry and to image them inside cells via confocal laser scanning microscopy. These results confirms that the intrinsic PL of carbonated ACP NPs can be effectively used for internalization assays and bioimaging procedures.

Conflicts of interest

There are no conflicts to declare.

Acknowledgements

The authors acknowledge the financial support of the following agencies: Fundação de Amparo à Pesquisa do Estado de São Paulo (FAPESP, Grants 2021/03559-5 and 2020/14417-4) and Conselho Nacional de Desenvolvimento Científico e Tecnológico (CNPq, Grant 164373/2020-9).

Notes and references

1 M. Vallet-Regí and J. M. González-Calbet, *Progress in Solid State Chemistry*, 2004, 32, 1–31.
2 S. V. Dorozhkin, *Biomater Sci*, 2021, 9, 7748–7798.
3 V. Sokolova and M. Epple, *Chemistry - A European Journal*, 2021, 27, 7471–7488.
4 C. Qi, S. Musetti, L. H. Fu, Y. J. Zhu and L. Huang, *Chem Soc Rev*, 2019, 48, 2698–2737.
5 A. Y. Cai, Y. J. Zhu and C. Qi, *Adv Mater Interfaces*, 2020, **7**, 2000819.
6 S. S. Syamchand and G. Sony, *Microchimica Acta*, 2015, 182, 1567–1589.
7 H. B. Shang, F. Chen, J. Wu, C. Qi, B. Q. Lu, X. Chen and Y. J. Zhu, *RSC Adv*, 2014, **4**, 53122–53129.
8 F. Chen, P. Huang, C. Qi, B. Q. Lu, X. Y. Zhao, C. Li, J. Wu, D. X. Cui and Y. J. Zhu, *J Mater Chem B*, 2014, **2**, 7132–7140.
9 I. Ortiz-Gómez, G. B. Ramírez-Rodríguez, L. F. Capitán-Vallvey, A. Salinas-Castillo and J. M. Delgado-López, *Colloids Surf B Biointerfaces*, 2020, **196**, 111337.
10 T. R. Machado, J. S. Silva, E. Cordoncillo, H. Beltrán-Mir, J. Andrés, V. Zucolotto and E. Longo, in *Research Topics in Bioactivity, Environment and Energy*, 2022, pp. 149–181.
11 C. Wang, K. J. Jeong, J. Kim, S. W. Kang, J. Kang, I. H. Han, I. W. Lee, S. J. Oh and J. Lee, *J Colloid Interface Sci*, 2021, **581**, 21–30.
12 K. Deshmukh, M. M. Shaik, S. R. Ramanan and M. Kowshik, *ACS Biomater Sci Eng*, 2016, **2**, 1257–1264.
13 T. R. Machado, I. S. Leite, N. M. Inada, M. S. Li, J. S. da Silva, J. Andrés, H. Beltrán-Mir, E. Cordoncillo and E. Longo, *Mater Today Chem*, 2019, **14**, 100211.
14 C. Zhang, C. Li, S. Huang, Z. Hou, Z. Cheng, P. Yang, C. Peng and J. Lin, *Biomaterials*, 2010, **31**, 3374–3383.
15 A. T. Simon, D. Dutta, A. Chattopadhyay and S. S. Ghosh, *ACS Appl Bio Mater*, 2021, **4**, 4495–4506.
16 M. Edén, *Materialia (Oxf)*, 2021, **17**, 101107.
17 A. S. Posner and F. Betts, *Acc Chem Res*, 1975, **8**, 273–281.
18 E. D. Eanes, *Calc. Tiss. Res.*, 1970, **5**, 133–145.
19 O. F. Yasar, W. C. Liao, B. Stevensson and M. Edén, *Journal of Physical Chemistry C*, 2021, **125**, 4675–4693.
20 V. Uskoković, S. Marković, L. Veselinović, S. Škapin, N. Ignjatović and D. P. Uskoković, *Physical Chemistry Chemical Physics*, 2018, **20**, 29221–29235.
21 R. Khalifehzadeh and H. Arami, *Adv Colloid Interface Sci*, 2020, **279**, 102157.
22 T. R. Machado, J. S. da Silva, R. R. Miranda, V. Zucolotto, M. S. Li, M. V. M. de Yuso, J. J. Guerrero-González, I. L. V. Rosa, M. Algarra and E. Longo, *Chemical Engineering Journal*, 2022, **443**, 136443.
23 C. Combes and C. Rey, *Acta Biomater*, 2010, 6, 3362–3378.
24 J. Vecstaudza, M. Gasik and J. Locs, *J Eur Ceram Soc*, 2019, **39**, 1642–1649.
25 D. Tadic, F. Peters and M. Epple, *Biomaterials*, 2002, **23**, 2553–2559.
26 R. Z. Legeros, *Nature*, 1965, **206**, 403–404.

27 M. J. Olszta, X. Cheng, S. S. Jee, R. Kumar, Y. Y. Kim, M. J. Kaufman, E. P. Douglas and L. B. Gower, *Materials Science and Engineering R: Reports*, 2007, 58, 77–116.

28 M. E. Fleet, *Carbonated hydroxyapatite: Materials, synthesis, and applications*, CRC Press, Boca Raton, 2015.

29 G. Gonzalez, C. Costa-Vera, L. J. Borrero, D. Soto, L. Lozada, J. I. Chango, J. C. Diaz and L. Lascano, *J Lumin*, 2018, **195**, 385–395.

30 D. L. Goloshchapov, P. V. Seredin, D. A. Minakov and E. P. Domashevskaya, *Optics and Spectroscopy*, 2018, **124**, 187–192.

31 T. R. Machado, J. C. Sczancoski, H. Beltrán-Mir, I. C. Nogueira, M. S. Li, J. Andrés, E. Cordoncillo and E. Longo, *J Solid State Chem*, 2017, **249**, 64–69.

32 C. Zollfrank, L. Müller, P. Greil and F. A. Müller, *Acta Biomater*, 2005, **1**, 663–669.

33 Y.-Y. Hu, A. Rawal and K. Schmidt-Rohr, *Proceedings of the National Academy of Sciences*, 2010, **107**, 22425–22429.

34 M. A. Martins, C. Santos, M. M. Almeida and M. E. V. Costa, *J Colloid Interface Sci*, 2008, **318**, 210–216.

35 E. Davies, K. H. Müller, W. C. Wong, C. J. Pickard, D. G. Reid, J. N. Skepper and M. J. Duer, *Proceedings of the National Academy of Sciences*, 2014, **111**, E1354–E1363.

36 B. Xie and G. H. Nancollas, *Proceedings of the National Academy of Sciences*, 2010, **107**, 22369–22370.

37 A. López-Macipe, J. Gómez-Morales and R. Rodrıb Guez-Clemente, *J Colloid Interface Sci*, 1998, **200**, 114–120.

38 J. M. Delgado-López, R. Frison, A. Cervellino, J. Gómez-Morales, A. Guagliardi and N. Masciocchi, *Adv Funct Mater*, 2014, **24**, 1090–1099.

39 S. C. G. Leeuwenburgh, I. D. Ana and J. A. Jansen, *Acta Biomater*, 2010, **6**, 836–844.

40 Y. Chen, W. Gu, H. Pan, S. Jiang and R. Tang, *CrystEngComm*, 2014, **16**, 1864–1867.

41 K. Chatzipanagis, M. Iafisco, T. Roncal-Herrero, M. Bilton, A. Tampieri, R. Kröger and J. M. Delgado-López, *CrystEngComm*, 2016, **18**, 3170–3173.

42 E. Ruiz-Agudo, C. Ruiz-Agudo, F. Di Lorenzo, P. Alvarez-Lloret, A. Ibañez-Velasco and C. Rodriguez-Navarro, *ACS Biomater Sci Eng*, 2021, **7**, 2346–2357.

43 J. Gómez-Morales, C. Verdugo-Escamilla, R. Fernández-Penas, C. M. Parra-Milla, C. Drouet, F. Maube-Bosc, F. Oltolina, M. Prat and J. F. Fernández-Sánchez, *RSC Adv*, 2018, **8**, 2385–2397.

44 Y. Jabalera, F. Oltolina, M. Prat, C. Jimenez-Lopez, J. F. Fernández-Sánchez, D. Choquesillo-Lazarte and J. Gómez-Morales, *Nanomaterials*, 2020, **10**, 199.

45 J. Gómez-Morales, R. Fernández-Penas, F. J. Acebedo-Martínez, I. Romero-Castillo, C. Verdugo-Escamilla, D. Choquesillo-Lazarte, L. D. Esposti, Y. Jiménez-Martínez, J. F. Fernández-Sánchez, M. Iafisco and H. Boulaiz, *Nanomaterials*, 2022, **12**, 1257.

46 A. Grunenwald, C. Keyser, A. M. Sautereau, E. Crubézy, B. Ludes and C. Drouet, *J Archaeol Sci*, 2014, **49**, 134–141.

47 V. Uskoković, *Vib Spectrosc*, 2020, **108**, 103045.

48 S. Krukowski, M. Karasiewicz and W. Kolodziejski, *J Food Drug Anal*, 2017, **25**, 717–722.

49 V. Uskoković, *Cryst Growth Des*, 2019, **19**, 4340–4357.

50 Z. Zyman, M. Epple, A. Goncharenko, M. Tkachenko, D. Rokhmistrov, D. Sofronov and H. Orlov, *Ceram Int*, 2024, **50**, 2185–2193.

51 J. D. Termine and D. R. Lundy, *Cult. Tiss. Res*, 1974, **15**, 55–70.

52 C. Ortali, I. Julien, C. Drouet and E. Champion, *Ceram Int*, 2020, **46**, 5799–5810.

53 J. M. Sedlak and R. A. Beebe, *J Colloid Interface Sci*, 1974, **47**, 483–489.

54 Y. Kojima, K. Sakama, T. Toyama, T. Yasue and Y. Arai, *Phosphorus Research Bulletin*, 1994, **4**, 47–52.

55 S. J. Gadaleta, E. P. Paschalis, F. Betts, R. Mendelsohn and A. L. Boskey, *Calcif Tissue Int*, 1996, **58**, 9–16.

56 P. C. H. Mitchell, S. F. Parker, K. Simkiss, J. Simmons and M. G. Taylor, *J Inorg Biochem*, 1996, **62**, 183–197.

57 L. Degli Esposti, M. Fosca, A. Canizares, L. Del Campo, M. Ortenzi, A. Adamiano, J. V. Rau and M. Iafisco, *Physical Chemistry Chemical Physics*, 2022, **24**, 24514–24523.

58 V. J. Huerta, P. Fernández, V. Gómez, O. A. Graeve and M. Herrera, *Appl Mater Today*, 2020, **21**, 100822.

59 T. R. Machado, J. C. Sczancoski, H. Beltrán-Mir, M. S. Li, J. Andrés, E. Cordoncillo, E. Leite and E. Longo, *Ceram Int*, 2018, **44**, 236–245.

60 V. S. Bystrov, C. Piccirillo, D. M. Tobaldi, P. M. L. Castro, J. Coutinho, S. Kopyl and R. C. Pullar, *Appl Catal B*, 2016, **196**, 100–107.

61 C. Lv, J. Zhang, L. Wu, G. Ouyang and X. Hou, *Carbohydr Polym*, 2023, **300**, 120235.

62 G. Blasse and B. C. Grabmaier, *Luminescent Materials*, Springer Berlin Heidelberg, Berlin, Heidelberg, 1994.

63 C. Cheng, K. Tong, Y. Fang, J. Wang, Y. Liu and J. Tan, *Coatings*, 2019, **9**, 289.

64 C. Zhang, Z. Cheng, P. Yang, Z. Xu, C. Peng, G. Li and J. Lin, *Langmuir*, 2009, **25**, 13591–13598.

65 D. Jiang, H. Zhao, Y. Yang, Y. Zhu, X. Chen, J. Sun, K. Yu, H. Fan and X. Zhang, *J Mater Chem B*, 2017, **5**, 3749–3757.

66 C. Qi, J. Lin, L. H. Fu and P. Huang, *Chem Soc Rev*, 2018, 47, 357–403.

67 T. Kataoka, S. Samitsu, M. Okuda, D. Kawagoe and M. Tagaya, *ACS Appl Nano Mater*, 2020, **3**, 241–256.

68 S. V. Dorozhkin, *Acta Biomater*, 2010, 6, 4457–4475.

69 S. M. C. Plá, A. D'urso, J. F. Fernández-Sánchez, D. Colangelo, D. Choquesillo-Lazarte, R. Ferracini, M. Bosetti, M. Prat and J. Gómez-Morales, *Nanomaterials*, 2022, **12**, 562.

70 E. Blanco, H. Shen and M. Ferrari, *Nat Biotechnol*, 2015, 33, 941–951.

71 B. O. Fowler, *Inorg Chem*, 1974, **13**, 194–207.
72 S. Somrani, C. Rey and M. Jemal, *J Mater Chem*, 2003, **13**, 888–892.
73 J. D. Termine, R. A. Peckauskas and A. S. Posner, *Arch Biochem Biophys*, 1970, **140**, 318–325.
74 M. Tagaya, T. Ikoma, S. Migita, M. Okuda, T. Takemura, N. Hanagata, T. Yoshioka and J. Tanaka, in *Materials Science and Engineering: B*, Elsevier BV, 2010, vol. 173, pp. 176–181.
75 T. Kataoka, T. Hashimoto, S. Samitsu, Z. Liu and M. Tagaya, *ACS Appl Nano Mater*, 2022, **5**, 2305–2315.
76 C. Zhang, J. Yang, Z. Quan, P. Yang, C. Li, Z. Hou and J. Lin, *Cryst Growth Des*, 2009, **9**, 2725–2733.
77 C. Wang, D. Liu, C. Zhang, J. Sun, W. Feng, X. J. Liang, S. Wang and J. Zhang, *ACS Appl Mater Interfaces*, 2016, **8**, 11262–11271.